Optical studies of 2D and 3D metallo-dielectric photonic crystals

Vladimir Kamaev, C. Liu, A. L. Pokrovsky, C. Y. Li, A. L. Efros and Z. Valy Vardeny*
Department of Physics, University of Utah, Salt Lake City, UT, USA 84112

ABSTRACT

We have fabricated and studied two-dimensional (2D) and three-dimensional (3D) metallo-dielectric photonic crystals (MDPC) in the visible/near ir spectral range using a variety of optical techniques. The 2D MDPC showed anomalous transmission due to surface plasmon polaritons in resonance with the photoluminescence band of a π-conjugated polymer based on a poly-phenylene-vinylene derivative. Consequently we fabricated an organic light emitting diode (OLED) using the 2D MDPC as a cathode with improved performance over an OLED with unperforated cathode. The 3D MDPCs are based on metal infiltrated opal photonic crystals. We studied the reflectivity spectrum of various metal infiltrated MDPCs and found that the reflectivity is low in the visible spectral range but dramatically increases towards the infrared revealing the elusive metallic gap. Our findings are in good agreement with recent theoretical and numerical calculations based on a commercial program.

Keywords: Metallo-dielectric photonic crystals, organic light emitting diodes, anomalous transmission, surface plasmon polaritons, opal photonic crystals, metal infiltrated opals, optical reflectivity and transmission spectra

1. INTRODUCTION

In this paper we review our studies of 2D and 3D MDPCs. The 2D MDPCs were in the form of thin metallic films perforated with hole arrays. We describe in section 2 our main finding, namely anomalous transmission mediated by surface plasmon polaritons on the two metallic/dielectric interfaces. We used the high optical transmission to fabricate an OLED based on the 2D MDPC as the cathode, and compare its characteristic properties with that of a reference OLED made with an unperforated cathode. In section 3 we describe our studies with 3D MDPCs that are opals infiltrated by different metals. We measured the optical reflectivity spectra and compared the experimental results with recent computer simulations. Based on the good agreement between theory and experiments we conclude that the main characteristic feature of 3D MDPCs is their metallic gap in the ir spectral range.

2. TWO-DIMENSIONAL METALLO-DIELECTRIC PHOTONIC CRYSTALS

2.1. Introduction

In the simplest form of OLED the active organic semiconductor is sandwiched between two metallic electrodes [1, 2]. Since such electrodes are usually opaque in the visible spectral range unless very thin, this type of geometry prevents efficient surface emission. This difficulty can be finessed, though by using a semitransparent electrode such as indium tin oxide (ITO) as the hole-injecting anode. In contrast for the electron-injecting cathode, opaque metallic electrodes such as aluminum (Al) are still been used [3]. In this OLED configuration, due to the relatively high refractive index of the organic active layer, a considerable fraction of the emitted radiation remains trapped in the device as waveguide modes that eventually couple to surface plasmons (SP) excitations on the anode surface, which consequently decay nonradiatively [4]. If nothing is done to recover this trapped waveguided light, then the device efficiency remains always low [5]. Recently we demonstrated [6] an efficient way to extract more electroluminescence (EL) light out of an OLED device using a semitransparent perforated electron-injecting cathode, due to the anomalous transmission caused by its patterned periodic two-dimensional (2D) subwavelength hole array that comprises of a 2D metallo-dielectric photonic crystal.

On a smooth metal-dielectric interface, light cannot efficiently couple to the SPP excitations, which are the elementary excitations of the metal surface, because conservation of energy, E and momentum, k are not obeyed [7]. On an (E, k) plot the SP dispersion curve lies below that of the electro-magnetic waves in vacuum [7]. But in a metal film that is

Plasmonics: Metallic Nanostructures and Their Optical Properties III, edited by Mark I. Stockman,
Proceedings of SPIE Vol. 5927 (SPIE, Bellingham, WA, 2005) · 0277-786X/05/$15 · doi: 10.1117/12.619879

perforated with a 2D periodic array of holes, the periodicity allows grating coupling of the SP to light [8]; this coupling results in surface plasmon polariton (SPP) excitations. The lattice periodicity promotes zone folding of the SP dispersion relation, which results in the formation of SP band structure that makes it possible for light to directly couple to SP excitations. Indeed it was recently found [8-18] that the optical transmission through subwavelength hole arrays fabricated on optically thick metallic films is enhanced at resonance wavelengths (or maxima), where light couples to the film's SPP excitations. If these maxima overlap with the photoluminescence (PL) band of the active organic layer of an OLED, then it might be possible to extract more EL light out of the device [5, 6, 19-21] without compromising the current injection capability of the patterned electrode.

Here we review our study [6] of the optical transmission, PL emission, OLED fabrication and electronic properties of an organic semiconductor polymer (a soluble derivative of poly-p-phenylene vinylene [PPV]) sandwiched between an optically thin gold anode, and an optically thick Al film perforated with a periodic hole array used as a cathode. We compare our results to those of a reference OLED based on an unperforated Al film with the same thickness. We found that the extraordinary transmission resonances in the Al optical spectra, which are well explained by light coupling to SPP excitations, match the PL band of the organic active layer, and thus more EL light could be extracted from the device. Indeed we obtained a seven-fold enhancement in the extracted EL light from the perforated Al device compared with that of the control OLED. We found that the enhancement factor is in agreement with the transmission enhancement through the Al electrode.

2.2. Experimental

The Al cathode hole array was in the form of a square 5x5 mm^2 in area that was fabricated by Nanonex Corp. (Princeton, NJ) using a nano-imprint method. The periodic hole array with square symmetry consisted of a 80 nm thick Al film on a glass substrate with subwavelength hole size of about 150 nm and lattice constant periodicity, a_0 of about 300 nm (Fig.1). The unperforated Al film used for the control OLED was fabricated by evaporating Al on glass, with the same thickness as that of the Al hole array sample. The active layer of both OLED's was a soluble derivative of PPV, namely poly (2-5 methoxy-ethyl-hexyloxy) [MEH-PPV] [6] (Fig. 5). The optical transmission spectra, $T(\lambda)$ through the films were measured at room temperature using a tungsten-halogen incandescent lamp, and a homemade spectrometer. The PL spectra of the MEH-PPV films deposited on the perforated and unperforated Al electrodes were measured at room temperature, in a cryostat under dynamic vacuum for protecting against photo-oxidation.

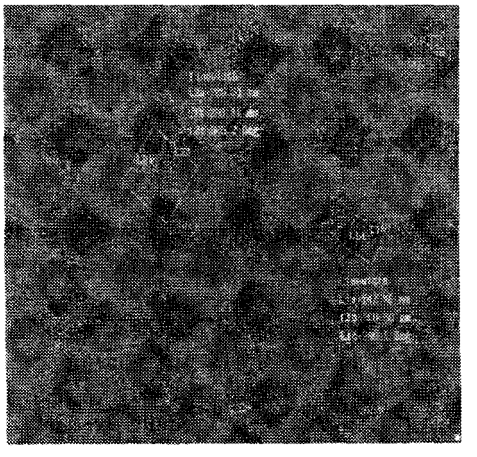

Figure 1: The 2D MDPC comprised of a 80 nm Al film perforated with a hole array of square symmetry, with holes 150 nm in size and lattice constant, a_0 of 300 nm.

The OLED's were fabricated by the "inverted method" [22], in which first the active layer is spin-coated on the cathode followed by deposition of the anode (Fig. 2). All procedures were done in a homemade glove box, having 1 ppm of oxygen. A thin layer (2 nm thick) of barium (Ba) was first evaporated onto the perforated Al and control Al films, for enhancing their electron-injection capability. We then spin-coated a 130 nm thick film of MEH-PPV onto the Al electrodes. The devices were completed by capping a 70 nm gold (Au), which was thermally evaporated using a shadow

mask in a vacuum chamber having a pressure of 10^{-6} torr. The I-V characteristics and the external EL quantum efficiencies (ELQE) of the devices were measured in a glove box that was purged with dry nitrogen using a computer-controlled Kiethley 236 source and measure unit, and an integrated sphere [23] with a silicon photodiode. The ELQE was calibrated using OLED's with known EL efficiency, which were obtained from another laboratory.

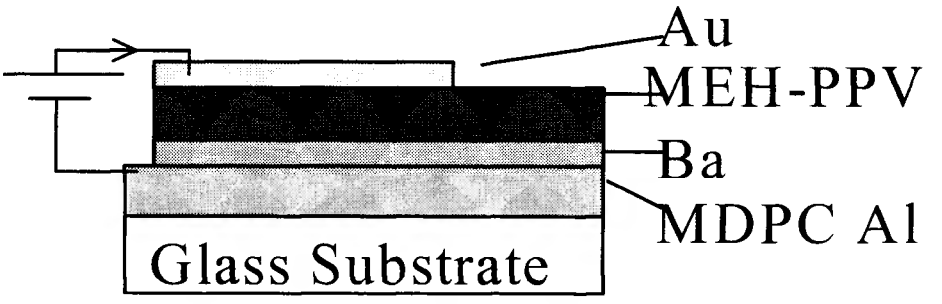

Figure 2: The OLED used in this work [6]. The active organic layer is a 130 nm thick MEH-PPV polymer with yellow emission; the anode is a 70 nm thick Au film; the cathode is a 80 nm thick Al or Al MDPC capped with a 2 nm thick Ba film on a glass substrate.

2.3. Results and discussion

The zeroth order optical transmission spectrum, T(λ) through the Al hole arrays in the visible/near-infrared spectral range is shown in Fig. 3 for an incident angle θ = 0. The spectrum is composed of several transmission resonances, λ_{max} and transmission minima, λ_{min}. The features at λ_{max} are due to extraordinary transmission resonances that are formed as the result of light coupling to SPP [8-18] giving T > 25% (which is the area covered by the holes in the perforated film). This could be verified from the angular dependence of T(λ), where a red shift in λ_{max} was measured at θ > 0. The transmission minima at λ_{min}, on the contrary are due to Wood's anomalies [24]. Importantly, T is maximum in the spectral range of MEH-PPV PL emission band (see Fig. 5 below), and thus the perforated film can be efficiently used to couple EL emission from the OLED [6, 25]. For comparison we plot in Fig. 3 T(λ) of the control Al film; T is very low, less than 1% in the spectral range of interest. We also plot in Fig. 4 T(λ) spectrum of the semi-transparent 70 nm thick gold electrode that was used as a cathode for the OLED devices. T(λ) peaks at 15%; but T at 600 nm, which is the PL emission maximum of the PPV-MEH polymer (Fig. 5) is only about 7%.

In the standard aperture theory of Bethe [26], the transmission through a sub-wavelength aperture follows $(d/\lambda)^4$ dependence due to diffraction, where d is the hole diameter. Therefore the transmission in our case should have been about 0.4%. However T(λ) through the Al sub-wavelength array of holes shows 'anomalous' behavior, with significant transmission at wavelengths much longer than d (Fig. 1(a)). The perforated metallic surface allows coupling between the incident light with H parallel to the surface and SPP excitations on both sides of the film. The conservation of momentum in this case can be written as [8],

$$\vec{k}_{sp} = \vec{k}_x \pm m\vec{u}_x \pm n\vec{u}_y, \qquad (1)$$

where $k_x = 2\pi/\lambda \sin\theta$ is the component of incident wave-vector of light in the plane of the hole array, $\vec{u}_x$ and $\vec{u}_y$ are the reciprocal lattice vectors (for a square lattice as in our case we have $u_x = u_y = 2\pi/a_0$), and m and n are integers. From the continuity of tangential H components E we get for the SP wave-vector, k_{sp} on a smooth metallic film

$$\left|\vec{k}_{sp}\right| = \frac{\omega}{c}\left(\frac{\varepsilon_m \varepsilon_d}{\varepsilon_m + \varepsilon_d}\right)^{\frac{1}{2}}, \qquad (2)$$

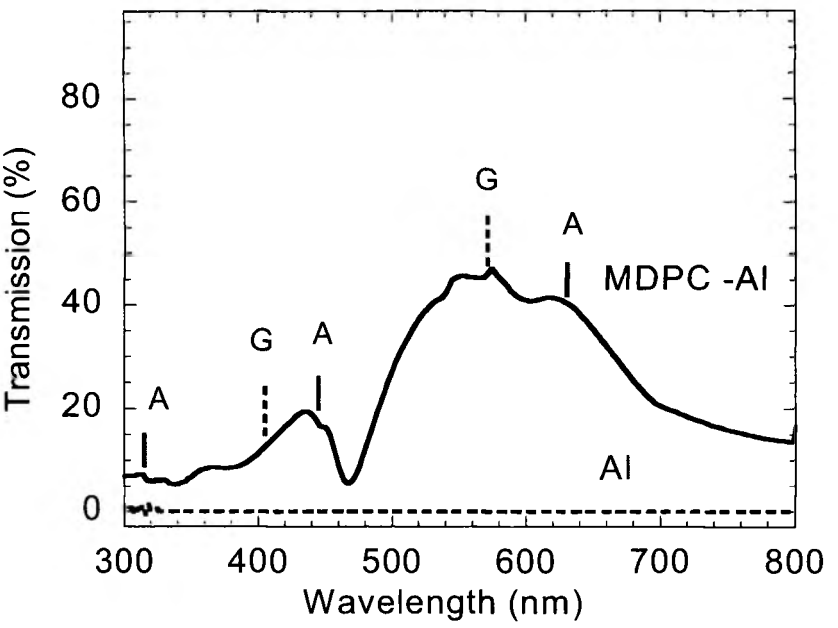

Figure 3: The optical transmission spectra, T(λ) of the 2D Al MDPC shown in Fig. 1. We compare T(λ) of the perforated Al (full line) to that of an unperforated Al film (dashed line). The anomalous transmission bands are assigned to the SPP excitations at the air-Al (G) or glass-Al (A) interfaces by vertical full lines and dashed lines, respectively [6].

where ε_m and ε_d are the real parts of the dielectric constants for the metal and substrate (glass or air), respectively, $\varepsilon_m<0$, $\varepsilon_d>0$, and $|\varepsilon_m| > \varepsilon_d$. At normal incidence ($\theta = 0$) Eqs. (1) and (2) can be reduced to

$$\lambda_{max} = \frac{a_0}{\sqrt{m^2+n^2}}\left(\frac{\varepsilon_m \varepsilon_d}{\varepsilon_m+\varepsilon_d}\right)^{\frac{1}{2}}. \qquad (3)$$

Using Eq. (3) the positions of the transmission maxima λ(n, m) may be associated with the SPP modes on the different interfaces (Fig. 3). However when taking for Al real(ε_m) = -54.3 at 633 nm and in the entire visible spectral range, we obtain transmission maximum due to the air-Al interface at λ(1, 0) = 300 nm; whereas the longest wavelength of transmission maximum due to air/Al interface is at 570 nm (Fig. 3). Same with the glass-Al interface; Eq. (3) gives maximum at λ(1, 0) = 430 nm, whereas the first transmission maximum for glass/Al interface occurs at 630 nm (Fig. 3). The transmission maxima are therefore *not in good agreement* with the theory. We note, however that the theory is good for describing holes with diameter much smaller that the lattice periodicity [9], which is not the case here. A much better fit between theory and experiment could be achieved if the effective real(ε_m) for the Al perforated film would have been much smaller than that for the bulk Al [6]. The transmission minimum at λ = 460 nm is due to Wood's anomaly [24], and thus cannot be described by coupling to SPP excitations.

The PL spectra of MEH-PPV spin-casted on the two Al films are shown in Fig 5 in both transmission and reflection geometries. The PL spectra (that are not normalized) show typical phonon replicas (0-n), and indicate that a good match exists with the transmission maxima of the perforated Al film (Fig. 3) [25], and that of the Au top electrode (Fig. 4). The PL intensity measured in transmission is relatively strong for the perforated Al electrode due to the match with the anomalous T(λ) spectrum. On the contrary, the PL intensity measured through the control Al film (not shown) is much smaller (by about two orders of magnitude).

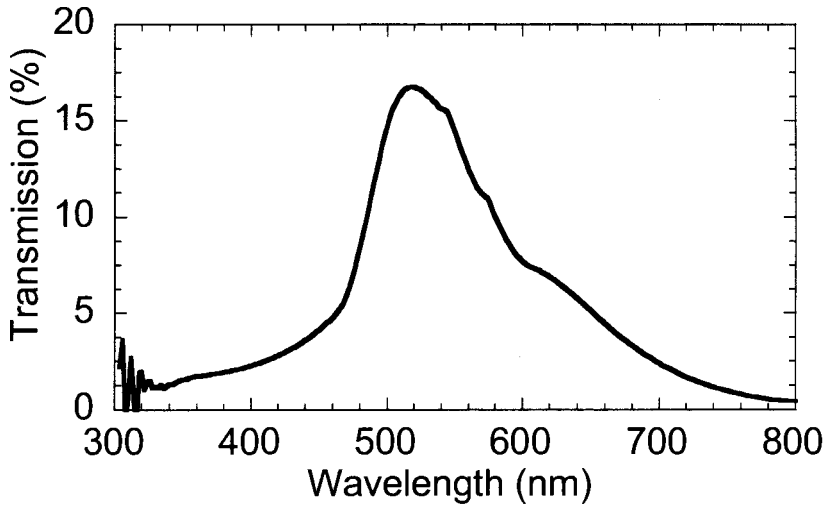

Figure 4: The transmission spectrum of a 60 nm thick Au film used as an anode in the fabricated OLED device.

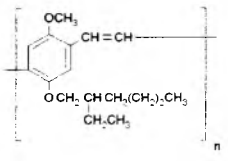

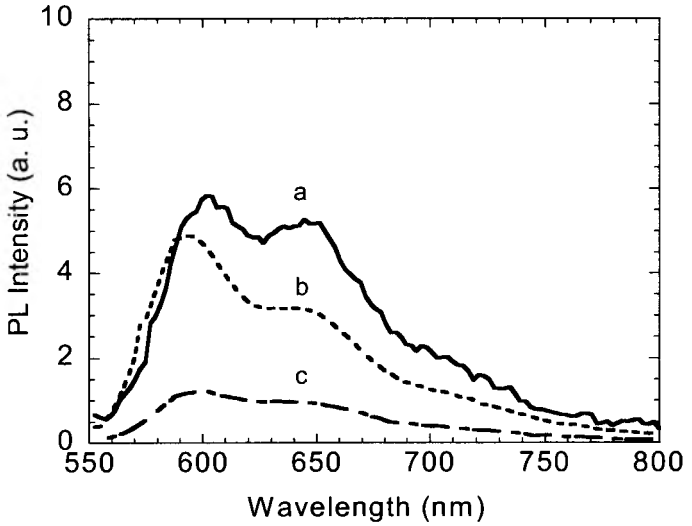

Figure 5: The PL spectra of a MEH-PPV polymer film spin coated on the unperforated Al (full line), and perforated Al electrodes, which are measured in reflection geometry (dashed line), and transmission geometry through the film (dotted-dashed line). The upper panel shows the MEH-PPV polymer repeat unit.

The measured responses of the two OLED's are shown in Figs. 6 and 7. Fig. 6 shows I-V characteristics; both devices show an abrupt onset to EL mode of operation. Clearly the device onset biasing voltage, V for the perforated Al ($V \approx$ 20 volt) is higher compared with that of the unperforated Al electrode ($V \approx 10$ volt). Nevertheless the I-V curves indicate that the perforated Al electrode, in principle can deliver as high current densities in spite of the many holes that decorate the electron-injecting cathode. Fig. 7 shows the ELQE of the two OLED's measured as a function of V. Admittedly the ELQE is low compared with the best values in the literature [3]. However we note that our devices do not have hole and electron intermediate transport layers, which, due to electron-hole balancing currents [3] can increase the ELQE by at least an order of magnitude. Importantly at similar current densities, J the OLED based on the perforated Al cathode shows a substantial ELQE enhancement over that based on the unperforated Al film, of up to a factor of seven at small J. At high J the enhancement is smaller, probably due to the patterned electron current density in the device that is injected by the hole arrays Al cathode.

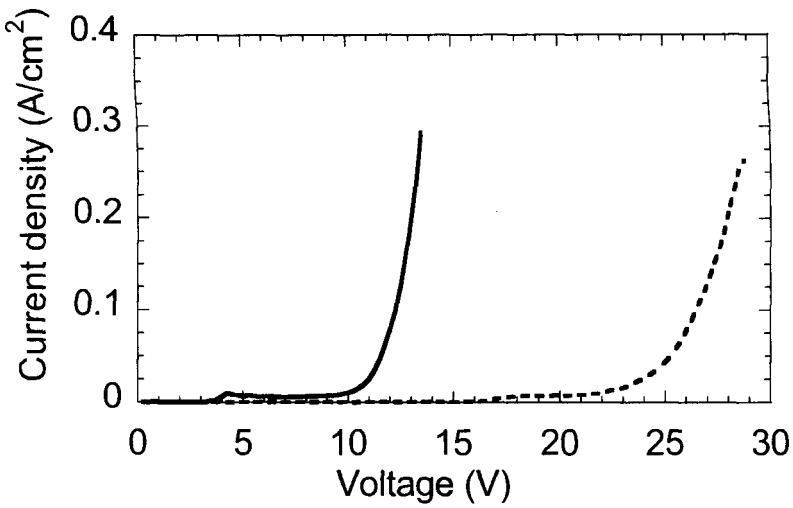

Figure 6: The I-V characteristics of the two OLED's; dashed (full) line is for the perforated (unperforated) Al cathode.

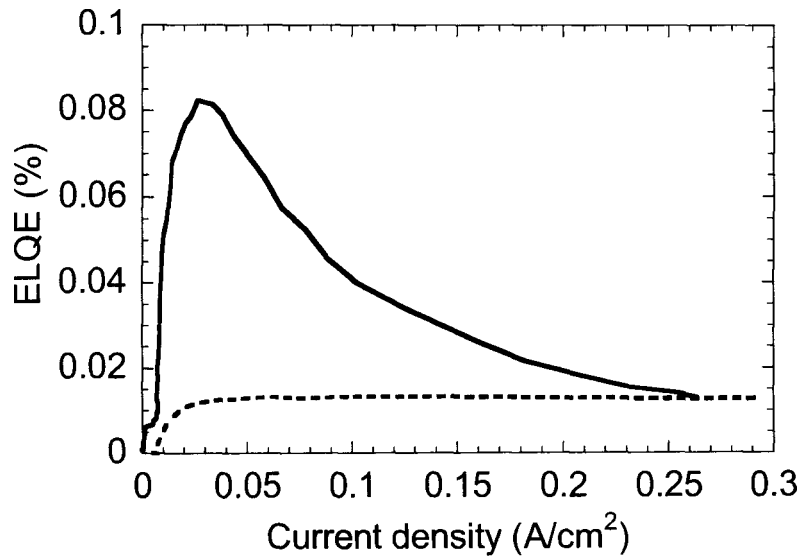

Figure 7: The EL quantum efficiency of the two OLED's as a function of the current density; dashed and full lines as in Fig. 6.

2.4. Conclusions

In conclusion we fabricated an OLED based on a perforated Al cathode in the form of a periodic 2D hole array, and compared its performance to that of a control device based on an unperforated Al electrode. The anomalous transmission through the patterned Al electrode can be well explained by resonant coupling of the incident light to SPP excitations on the two cathode interfaces, and matches the PL emission spectrum of the active polymer, MEH-PPV. At similar current densities we obtained up to seven-fold increase in the EL collection efficiency from the perforated device compared to the control device. This demonstrates that the method of patterning the electrodes into 2D hole arrays is very efficient, and can be used in the future for extracting more EL in practical device applications.

3. THREE-DIMENSIONAL METALLO-DIELECTRIC PHOTONIC CRYSTALS

3.1. Introduction

The idea underlying our studies of 3D metallic photonic crystals [27] is to create a medium with metallic dc conductivity and, at the same time with transparency to electromagnetic (EM) waves in a desire frequency range. We review here our theoretical, numerical and experimental studies of the optical properties of opal photonic crystals infiltrated with various metals. The optical spectrum of 3D MDPC differs dramatically from a dielectric photonic crystal in a low frequency range. A dielectric crystal has a propagating mode with a wavelength larger than the period, d of the crystal. The dispersion relation of this mode is similar to that of light in vacuum, $\omega = ck/\sqrt{\varepsilon_{av}}$ where ε_{av} is the average dielectric constant of the medium. This mode reaches zero frequency at very long wavelength.

On the contrary the optical spectrum of 3D MDPCs has an important and interesting feature, namely a cutoff frequency ω_c. For $\omega < \omega_c$ there are no propagating EM modes [28, 29]. The explanation of this phenomenon is as follows. If the EM wavelength is much larger than the period d of the MDPC, then the macroscopic dielectric constant, $\varepsilon(\omega)$ explored by the wave is the averaged dielectric constant of the metallic and dielectric constituents of the MDPC structure. Therefore the complex $\varepsilon(\omega)$ has the form

$$\varepsilon(\omega) = (1-f)\varepsilon_d + fi\sigma/\omega, \qquad (4)$$

where ε_d refers to the dielectric, σ is the metal's optical conductivity, and f is the volume filling fraction of the metal. It is apparent that at small ω, ε is imaginary and thus R = 1; consequently no EM waves can propagate into the MDPC at such frequencies. In this model the MDPC is treated as a homogeneous metal with electron density fn, where n is the electron density of the metal. It is obvious that the cutoff frequency in this model is $\omega_c = \omega_p\sqrt{f}$ where ω_p is the plasma frequency of a metal.

However, taking into account the real structure of 3D MDPC, we can easily find the spectrum of the EM modes below this frequency. Their fields must be in the form of periodic Bloch functions, and thus propagation becomes possible because the distribution of electric field in the elementary cell is such that the field is small at the surfaces of the metallic constituents. However, such a modulation increases the EM frequency so that the spectrum would have a cutoff frequency of the order of $\omega_c \approx 2\pi c/\sqrt{\varepsilon_d}d$ [28, 29]. Consequently, ω_c is determined by the MDPC lattice constant; for MDPC's with period of the order of millimeters, ω_c is in the GHz range. To fabricate 3D MDPC operating in the visible spectral range the lattice constant should be ~250 nm [30 – 33].

One of the most promising 3D MDPC structures with such a small period are metal infiltrated opals (MIO) [30]. Opal is a close-packed fcc photonic crystal formed by silica balls with a diameter D between 250 and 1500 nm [30 – 36]. The volume fraction of the empty pores in a bare, uninfiltrated opal is ≈ 26%. The structure of a bare opal photonic crystal and the dispersion of EM waves are shown in Fig. 8. We can see the low energy mode typical of a dielectric photonic crystal. The first computational study of opal replica (where the silica balls are substituted by silver) was done by Moroz [37]. The first optical studies of reflectivity in MIO were completed on Bi infiltrated opals [38], followed by Ga MIO [39]. Recently, tungsten inverse opals were experimentally studied [40]. The EM dispersion relations of uniaxial

crystals consisting of metallic wires can be studied analytically [29, 41]. However, the opal geometry is so much more complicated that only numerical computations are possible; these were recently performed at the University of Utah in our group using a commercial software package [42].

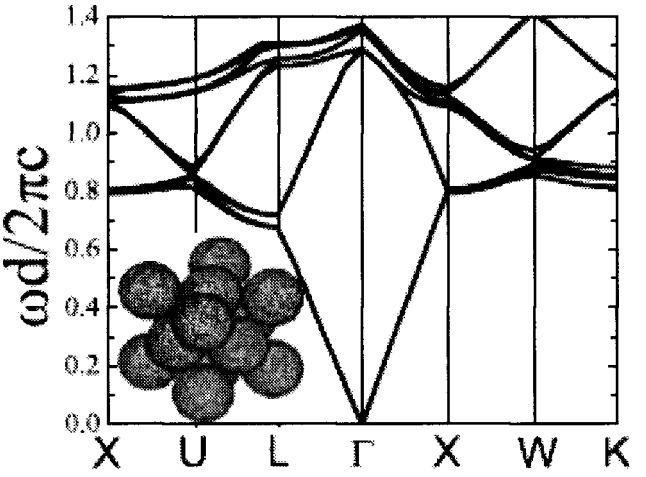

Figure 8: EM dispersion relation calculated using FEMLAB. The opal cubic cell is shown in the inset. Various high symmetry points in the inverse Bravais lattice are assigned along **k** axis.

3.2. Theoretical Studies of Metal Infiltrated Opals

3.2.1. Photonic spectra of metal infiltrated opals

We start by considering a simple model of opal infiltrated by an "ideal" metal. In this approximation the metal in the frequency range of interest is described by a dielectric constant with a large, negative real part, and small imaginary part. We also assume that the infiltration factor p is close to 1. This means that all empty pores of the opal photonic crystal are completely filled by the metal; consequently, the volume filling fraction of the metal is $f = 0.26$. In this case we may neglect the frequency response of the metallic dielectric constant, because the EM fields do not penetrate into the metal. The resulting EM dispersion relations are shown in Fig. 9a. They have a simple quantitative interpretation, and may serve as a reference point for interpreting EM band structures in the case of real metal infiltration.

An ideal MIO system can be considered as a periodic array of spherical cavities filled by silica and covered by a metal. Since the metal quality is excellent, each cavity represents a high-Q resonator. In this case the fields are mostly localized inside the cavities, and the interaction between cavities is very weak. Therefore the dispersion of the propagating EM modes is negligible small and their frequencies almost coincide with the eigenfrequencies of an ideal spherical cavity filled with silica. The lowest eigenfrequency of such a cavity is $\omega_c \approx 5.48c/\sqrt{\varepsilon_d}D$, where ε_d is the dielectric constant of silica [43]. This mode is three-fold degenerate since it corresponds to the angular momentum l = 1. The next mode, $\omega \approx 7.78c/\sqrt{\varepsilon_d}D$ is five-fold degenerate (l = 2). In MIO with a real metal this degeneracy is lifted due to interaction with neighboring cavities.

Computations of photonic band structures for opals infiltrated with real metals are more complicated due to the frequency dispersion of the dielectric constant, which was taken from the literature [44]. A simple interactive procedure was used and it provides solutions with a good convergence and stability. Figure 9b demonstrates the calculated photonic band structure of Ag infiltrated opal with p = 1 and D = 285 nm. The EM dispersion was found to be larger than in the case of an "ideal" metal, but is still small. The resonator eigenfrequencies are lower for larger diameter silica spheres; metal at such frequencies is closer to being perfect. Therefore the EM dispersion decreases with increasing D. We conclude this part with the claim that the characteristic property of EM dispersion relation in opal

infiltrated with a 'good' metal is that they are very narrow having small group velocity. Also the fields are mostly concentrated in the silica cavities.

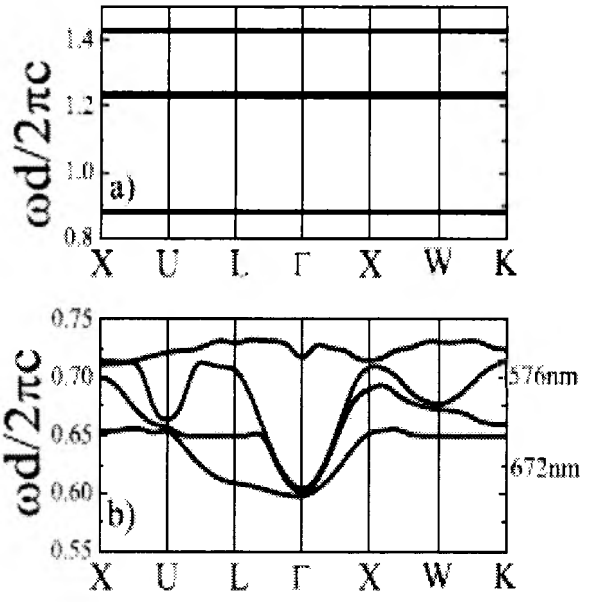

Figure 9: Lowest dispersion relations of EM waves in opal with silica ball diameter of 285 nm infiltrated with ideal metal (a) and silver (b).

3.2.2. Reflectivity and transmission spectra of MIO

Reflectivity, R(ω) and transmission, T(ω) spectra of MIO's were calculated for silver and lead. We considered a monochromatic plane wave at normal incidence with respect to the MIO crystals, which are cut perpendicular to <100> directions. Figure 10 shows R and T spectra for five layer silver and three layer lead infiltrated opals, respectively with $p = 1$ and $D = 285$ nm. The main feature in R(ω) is the growth and saturation at long wavelength, which is due to the low frequency gap in the photonic spectra of MIO's. The fist minimum in R(ω) and maximum in T(ω) appear due to the existence of propagating EM modes above the cutoff frequency. In fact the MIO samples that were prepared experimentally were cut perpendicular to <111> rather than <100> direction. Nevertheless, the frequency region of the propagating EM modes is so narrow that the first minima in reflectivity should be isotropic. The vertical lines in Fig. 10 show the positions of ω_Γ and ω_X from the photonic band structure given in Fig. 9.

For comparing the computational results with the experimental reflectivity spectra we took into account that the actual opal samples do not have $p = 1$. Therefore the following computational model for the actual MIO's was created. We started with a close packed fcc lattice of 285 nm silica spheres, and increased D while keeping the lattice constant unchanged. This procedure was designed to create the nearest neighbor spheres' overlap, while at the same time the volume fraction of the pores decreased to ≈ 16 %, whereas the pores were filled by metal (the volume fraction of metal in this system corresponds to an opal with $p = 0.6$). Reflectivity and transmission spectra of this new model when filled with Ag are shown in Fig. 10c. Since the new MIO has less metal compared to opal with $p = 1$, the cutoff frequency is lower and the dispersion of the propagating bands is larger. These qualitative results follow from the model of spherical cavities considered above. Consequently, the first minimum in R(ω) (Fig. 10c) occurs at a longer wavelength compared with that in Fig 10a.

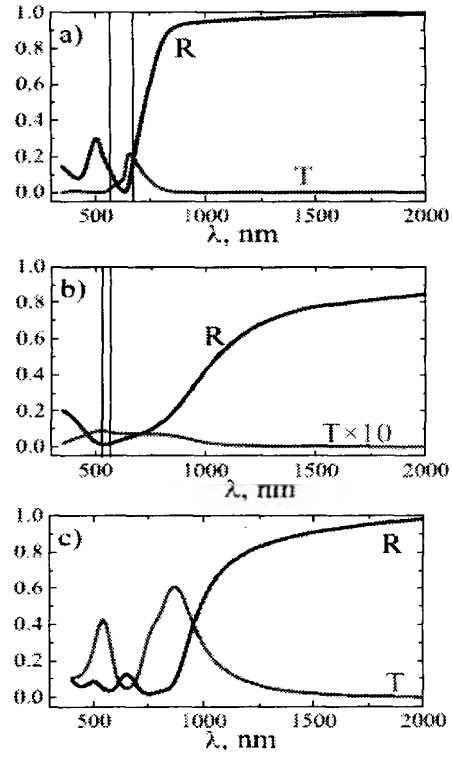

Figure 10: Calculated reflectivity, R and transmission, T spectra of MIO's with silica ball diameter of 285 nm infiltrated with silver (a) and lead (b) having relative filling factor p = 1. (c) Same as in (a) but for filling factor p = 0.6.

3.3. Optical Studies of Metal Infiltrated Opals

We have fabricated 3D MIO's that consist of infiltrated metals into porous synthetic opal photonic crystals. Two different metals were chosen for the opal infiltration: silver and copper, both having typical metallic properties. The specular reflectivity of the infiltrated and uninfiltrated opals, as well as the pure metals was subsequently measured in a broad spectral range from 0.3 to 25μm using several combinations of light sources, detectors and spectrometers. We found that the optical reflectivity spectra of the MIO samples dramatically decrease in the visible/NIR spectral range, recuperating in the mid-IR range below a cutoff frequency. In addition, some of the MIO samples showed relatively bright iridescence colors caused by a broad Bragg stop band in the visible range that was formed due to the enhanced optical penetration depth in the composites, compared to the skin depth of the pure metals.

3.3.1. MIO fabrication

Opal PC's as templates for the metal infiltration were grown by our collaborators at St Petersburg using sedimentation of 245, 285 and 550 nm diameter silica-balls, respectively in aqueous solutions. The resulting synthetic opals consisted of micro-crystals with characteristic size of tens of micrometer and a preferable vertical orientation along the <111> crystallographic direction. Silver and copper were introduced into the bare opal matrix by the chemical bath deposition method [45]. First, the interconnected pore sublattice in the opal sample was impregnated by saturated aqueous solutions of $AgNO_3$ or $Cu(NO_3)_2$. The samples were dried and the salts were reduced by hydrogen. The rate of the hydrogen flow was about 1sccm (cubic centimeter per minute) and the reduction process temperature was 400°C for both metals. We repeated this procedure periodically to increase the infiltration factor of the opal pores.

The infiltration factor that was controlled by the gravimetric technique was found to be $p = 0.6 \pm 0.05$ for both metals. The results of the gravimetric measurements are reasonable because these metals have much larger densities (Ag-10.5g/cm^3, Cu – 8.9g/cm^3) compared with bare opals (1.3 g/cm^3), and this reduces the uncertainties in determining p.

The resulting MIO samples were approximately 5 x 5x 1 mm^3 with the flat surface area perpendicular to <111>; these samples were finely polished to be suitable for the specular reflectivity measurements. The obtained MIO's were electrically conductive showing network topology. We performed additional estimates of the metal filling factor by several techniques including measurement of the average density, and also reversing the infiltration by dissolving the metal. We found that the infiltration factor p for Ag and Cu MIO's was 0.6 ± 0.1, in good agreement with p obtained from the gravimetric measurements.

3.3.2. Optical Measurements

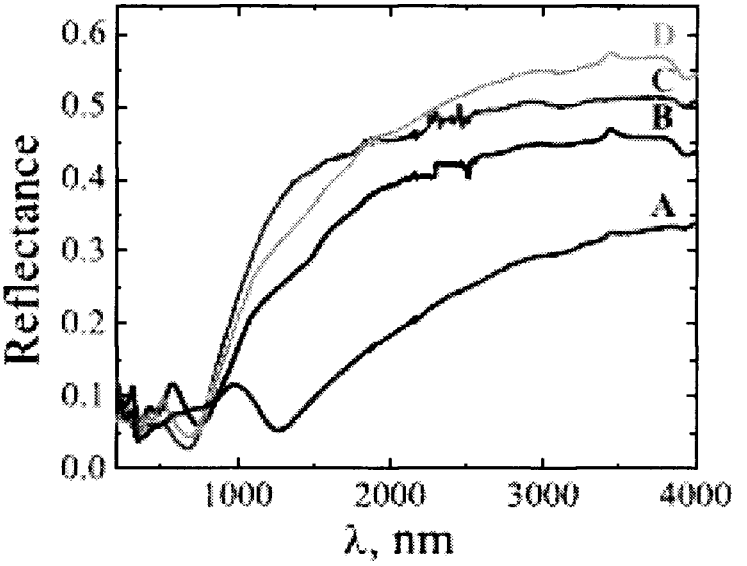

Figure 11: Reflectivity spectra of MIO's; all MIO's have filling p = 0.6. A - Ag, D = 550 nm; B – Ag, D = 285 nm; C – Cu, D = 245 nm; D – Ag, D = 245 nm.

The specular reflectivity, R(ω) from 0.3 to 4.1 μm was measured for the MIO's, metallic films and uninfiltrated opal samples using a homemade spectrometer. The spectrometer consists of various incandescent light sources (tungsten-halogen and glow-bar lamps), solid-state detectors (enhanced-UV Si, Ge, and InSb), and a 0.3-met. monochromator (Action Research Corporation) that was equipped with several gratings in order to span the required broad spectral range. The measured R(ω) spectra were also compared with R(ω) obtained using a Fourier transform infrared spectrometer in the mid-IR spectral range of 2-25μm, by normalizing the spectra at the overlapping spectral range. The incident light beam was directed to be about 13° with respect to the surface normal. The obtained R(ω) spectra were normalized by that of a gold platted mirror measured under the same conditions at the respective spectral ranges. The MIO samples were kept at ambient during the measurements. A comparison with reflectivity spectra measured using an integrating sphere was also done. The integrating sphere measures the specular as well as the diffused reflectivity.

Figure 11 shows the reflectivity spectra of four MIO samples, Ag infiltrated in opals of various silica ball diameters, and Cu infiltrated into opal of 245 nm ball diameter. R(ω) of all four samples is small in the visible spectral range showing that the EM radiation may indeed penetrate into the MIO's at these short wavelengths. R(ω) increases at long wavelengths for all four MIO samples with a threshold at a cutoff wavelength λ_c. λ_c for the three MIO samples with the smaller diameter is about the same at ≈ 700 nm; although λ_c for the smallest silica ball opal is the shortest. For the 550

nm diameter MIO λ_c is about 1300 nm. This agrees well with the ratio between the silica ball diameters of the various MIO samples. We get $\lambda_{c,b} / \lambda_{c,s} \approx D_b / D_s \approx 1.9$, where $\lambda_{c,b}(\lambda_{c,s})$ is λ_c for the MIO with the big D_b (small D_s) silica ball diameter; this is in good agreement with the simple model presented above in the introduction. We conjecture that $R(\omega)$ general appearance and cut-off wavelengths are in very good agreements with the calculated spectra presented in Fig. 10 above.

3.3.3. Conclusions

In summary, we have shown that the optical properties of synthetic opal photonic crystals infiltrated with metals can be qualitatively understood using a simple model of weakly interacting spherical resonators. Photonic band structures for opals infiltrated with Ag and Pb were calculated, where the dielectric constant dispersion of the metal was taken into account. The propagating EM bands are narrow and for good metals they are separated by an omnidirectional band gap. Reflectivity and transmission spectra for thin film MIO's were calculated for Ag and Pb infiltrated opals. Opal samples were fabricated and infiltrated by Ag and Cu using the chemical bath deposition method. Reflectivity spectra were measured in the visible and mid-IR spectral range and were found to be in a good agreement with the computational results.

ACKNOWLEDGEMENTS

We are grateful to our collaborators Drs. D. A. Kurdyukov and V. G. Golubev at the Ioffe Physico-Technical Institute in St. Petersburg for the MIO's preparation, and Drs. J. Shi and S. Blair for fruitful discussions. The work was funded by the ARO grant DAAD 19-03-1-0290 and the DOE grant # FG-02-04ER46109.

REFERENCES

1. C. W. Tang, and S. A. VanSlyke, Appl. Phys. Lett. 51, 913 (1987).
2. J. H. Borroughes, D. D. C. Bradley, A. R. Brown, R. N. Marks, K. MacKay, R. H. Friend, P. L. Burn, and a. B. Holmes, Nature (London) 347, 799 (1990).
3. R. H. Friend, R. W. Gymer, A. B. Holmes, J. H. Burroughes, R. N. Marks, C. Taliani, D. D. C. Bradley, D. A. Dos Santos, J. L. Bredas, M. Logdlung, and W. R. Salaneck, Nature (London) 397, 121 (1999).
4. P. A. Hobson, J. A. E. Wasey, I. Sage, and W. L. Barnes, IEEE Selec. Top. Quantum Elect. 8, 378 (2002).
5. W. L. Barnes, P. A. Hobson, S. Wedge, J. A. E. Wasey, and I. Sage, Adv. Mater. 14, 1393 (2002).
6. C. Liu, V. Kamaev, and Z. V. Vardeny, Appl. Phys. Lett. 86, 143501 (2005).
7. H. Raether, *Surface Plasmons on Smooth and Rough Surfaces and on Gratings*, Springer-Verlag, Berlin, 1988.
8. T. W. Ebbesen, H. J. Lezec, H. F. Gaemi, T. Thio, and P. A. Wolff, Nature (London) 391, 667 (1998).
9. T. Thio, H. F. Ghaemi, H. J. Lezec, P. A, Wolff and P. A. Ebbesen, J. Opt. Soc. Am. B 16, 1743 (1998).
10. T. J. Kim, T. Thio, T. W, Ebbesen, D. E. Grupp, and H. J. Lezec, Opt. Lett. 24, 256 (1999).
11. Avrutsky, Y. Zhao, and V. Kochergin, Opt. Lett. 25, 595 (2000).
12. D. E. Grupp, H. J. Lezec, T. W. Ebbesen, K. M. Pellerin, and T. Thio, Appl. Phys. Lett. 77, 1569 (2000).
13. L. Martin-Moreno, F. J. Garcia-Vidal, H. J. Lezec, K. M. Pellerin, T. Thio, J. B. Pendry, and T. W. Ebbesen, Phys. Rev. Lett. 86, 114 (2001).
14. L. Salomon, F. Grillot, A. V. Zayats, and F. de Fornel, Phys. Rev. Lett. 86, 1110 (2001).
15. A. M. Dykhne, A. K. Sarychev, and V. M. Shalaev, IEEE Jour. Quantum Elect. 38, 956 (2002).
16. S. Enoch, E. Popov, M. Nevier, and R. Reinisch, J. Optics A: Pure Appl. Opt. 4, S83 (2002).
17. A. Krishnan, T. Thio, T.J. Kim, H.J. Lezec, T.W. Ebbesen, P.A. Wolff, J. Pendry, L. Martin-Moreno, and F.J. Garcia-Vidal , Opt. Commun. 200, 1 (2002).
18. Y. Liu and S. Blair, Opt. Lett. 28, 507 (2003).
19. S. Gianordoli, R. Hainbrerger, A. Kock,, N. Finger, E. Gornik, C. Hanke, and L. Korte, Appl. Phys. Lett. 77, 2295 (2000).
20. D. K. Gifford and D. G. Hall, Appl. Phys. Lett. 81, 4315 (2000); *ibid* 80, 3679 (2002).
21. H. Ichikawa and T. Baba, Appl. Phys. Lett. 84, 457 (2004).
22. T. Dobbertin, O. Werner, J. Meyer, A. Kammoun, D. Schneider, T. Riedl, E. Becker, H. –H. Joannes, and W.

Kowalski, Appl. Phys. Lett. 83, 5071 (2003).
23. N. C. Greenham, I. D. W. Samuel, G. R. Hayes, R. T. Phillips, Y. A. R. R. Kessener, S. C. Moratti, A. B. Holmes, and R. H. Friend, Chem. Phys. Lett. 241, 89 (1995).
24. R. W. Wood, Philos. Mag. 4, 396 (1902); *Proc. R. Soc. London A* 18, 269 (1902).
25. As a matter of fact T(λ) slightly changes after the polymer deposition; however when the angular dependence of the first maximum is taken into account, then it efficiently cover the entire PL spectrum.
26. H. A. Bethe, *Phys. Rev.* 66, 163 (1944).
27. A. L.Pokrovsky, V. Kamaev, C. Y. Li, Z. V. Vardeny, A. L. Efros, D. A. Kurdynkov, and V. G. Golubev, Phys. Rev. B 71, 165114 (2005).
28. J. B. Pendry, A. J. Holden, W. J. Stewart, and I. Youngs, Phys. Rev. Lett. 76, 4773 (1996).
29. A. L. Pokrovsky and A. L. Efros, Phys. Rev. Lett. 89, 093901 (2002).
30. A. A. Zakhidov, R. H. Baughman, Z. Iqbal, C. Cui, I. Khayrullin, S. O. Dantas, J. Marti, and V. G. Ralchenk, Science 282, 897 (1998).
31. B. T. Holland, C. F. Blanford, and A. Stein, Science 281, 538 (1998).
32. O. D. Velev, P. M. Tessier, A. M. Lenhoff, and E. W. Kaler, Nature (London) 401, 548 (1999).
33. J. E. G. J. Wijnhoven, S. J. M. Zevenhuizen, M. A. Hendriks, D. Vanmaekelbergh, J. J. Kelly, and W. L. Vos, Adv. Mater. (Weinheim, Ger.) 12, 888 (2000).
34. V. G. Golubev, J. L. Hutchison, V. A. Kosobukin, D. A. Kurdyukov, A. V. Medvedev, A. B. Pevtsov, J. Sloan, and L. M. Sorokin, J. Non-Cryst. Solids 299, 1062 (2003).
35. C. Lopez, Adv. Mater. (Weinheim, Ger.) 15, 1679 (2003).
36. B. T. Mayers, B. Gates, and Y. Xia, Adv. Mater. (Weinheim, Ger.) 12, 1629 (2000).
37. A. Moroz, Phys. Rev. Lett. 83, 5274 (1999).
38. N. Eradat, J. D. Huang, Z. V. Vardeny, A. A. Zakhidov, I. Khairullin, I. Udod, and R. H. Buaghman, Synth. Met. 116, 501 (2001).
39. V. Kamaev, V. Kozhevnikov, Z. V. Vardeny, P. B. Landon, and A. A. Zakhidov, J. Appl. Phys. 95, 2947 (2004).
40. G. Freymann, S. John, M. Schultz-Dobrick, E. Vekris, N. Tetreault, S. Wong, V. Kitaev, and G. A. Ozin, Appl. Phys. Lett. 84, 224 (2004).
41. A. L. Pokrovsky and A. L. Efros, Phys. Rev. B 65, 045110 (2002).
42. FEMLAB, *Reference Manual, Version 2.2* (Comsol AB, Sweden, 1994).
43. L. D. Landau and E. M. Lifshitz, *Electrodynamics of Continuous Media* (Pergamon Press, Oxford, 1960).
44. M. A. Ordal, L. L. Long, R. J. Bell, S. E. Bell, R. R. Bell, R. W. Alexander, and C. A. Ward, Appl. Opt. 22, 1099 (1983).
45. V. G. Golubev, V. Yu. Davydov, N. F. Kartenko, D. A. Kurdyukov, A. V. Medvedev, A. B. Pevtsov, A. V. Scherbakov, and E. B. Shadrin, Appl. Phys. Lett 79, 2127 (2001).